Understanding Kinetically Controlled Spin Transitions in Bistable Spin Crossover Materials

Sergi Vela, Maria Fumanal, Carmen Sousa*

ª Departament de Ciència de Materials i Química Física and IQTCUB, Universitat de Barcelona, Martí i Franquès 1, E-08028, Barcelona, Spain. sergi.vela@ub.edu

S1. Methodology

S1.1. Grid Generation

The grid of points (geometries) at which the HS, LS and IS energies are calculated is generated as follows. First, the coordinates of the minima of the HS and IS states are represented on the basis of the dimensionless Q coordinates of the Vibrational Normal Modes (VNM) of the LS minima (ν_i^{LS}) (without rotation and translation modes), obtaining a set of displacements for each VNM i and state l (Q_i^l). To transform between cartesian and Q coordinates, we use eq. S1:

$$\mathbf{Q} = \widetilde{\mathbf{D}}(\mathbf{x} - \mathbf{x}^{LS}) \qquad (S1)$$

where the transformation matrix $\widetilde{\mathbf{D}}$ contains the mass-weighted eigenvectors of the LS state.

Second, the Hessian of the HS and IS states are projected on the Hessian of the reference state (LS). From the projected matrices, we extract the diagonal terms (ω_i^l), which represent the frequency of state l along the dimension of the LS VNM i. From these, we estimate the stabilization energy associated with each mode using the harmonic approximation, and the energy gradient of state l at the LS minimum (κ_i^l) ($E_{vert,i}^l$, see eq. S2).

$$E_{vert,i}^l = -\frac{1}{2}\frac{(\kappa_i^l)^2}{\omega_i^l} \qquad (S2)$$

Our notation follows that of the Linear Vibronic Coupling (LVC) model.[1] In this case the HS, LS and IS states represent diabatic states without interstate coupling, thus they coincide with the adiabatic states. The VNM associated with the largest $E_{vert,i}^l$ values are the dimensional coordinates that stabilize more the HS and IS minima far from the LS reference. The four VNM with largest values are taken as *main* dimensions of the grid, and the remaining ones are considered altogether in a single dimension, that is called the *combined* mode. For each mode, the range of Q_i explored in the grid must include its minimum and maximum value among states (Q_i^{MIN} and Q_i^{MAX}). For instance, if $Q_i^{LS} = 1$, $Q_i^{IS} = 0$ and $Q_i^{HS} = 2$ for a given VNM, the range explored in the grid needs to be, at least, from 0 to 2. In our case, we have allowed some margin at the extremes, so the initial and final Q_i are defined as:

$$Q_i^{ini} = Q_i^{MIN} + \frac{(Q_i^{MIN} - Q_i^{MAX}) \cdot B}{2} \qquad (S3a)$$

$$Q_i^{fin} = Q_i^{MAX} + \frac{(Q_i^{MAX} - Q_i^{MIN}) \cdot B}{2} \qquad (S3b)$$

where B is the *boundary* parameter. We took $B=0.5$, which implies that the actual range of Q_i is extended by a 50% (from −0.5 to 2.5 in the example above). The number of points (N_i) explored in each direction is defined as eq. S4

$$N_i = MAX\left(1 + \frac{Q_i^{fin} - Q_i^{ini}}{M}; 1\right) \qquad (S4)$$

where M is a variable that defines the point separation, and $(Q_i^{fin} - Q_i^{ini})$/M is approximated to the larger integer. For the *ab-initio* grid, in which all geometries are evaluated from electronic structure computations, we took *M=3.5,* and hence equation S4 yields $N_i = 3,3,7,3$ for the *main* modes (see Table S1). For the *combined* mode, we computed 7 equidistant points ($N_C = 9$) in which Q_i of each of the 143 contributing modes is simultaneously and proportionally increased from the minimum to the maximum values (see Table S1). The entire grid consists of 1323 points, whose geometry in cartesian coordinates is obtained considering the displacement in Q associated with each VNM (Q_i) to the reference LS geometry by rearranging eq. S1 into:

$$\mathbf{x} = \mathbf{x}^{LS} + \widetilde{\mathbf{D}}'\mathbf{Q} \qquad (S5)$$

The *main* VNM of $[Fe^{II}(1\text{-}bpp)_2]^{2+}$ (**1**) describe a change in the Fe-N coordination sphere through the modification of the Fe-N(pyr) and Fe-N(pz) distances, as well as the distortion motion characteristic of Fe^{II}-bpp complexes (see Section 2 of the main text). These

4 normal modes retrieve a $E_{vert,i}^l$ of 1.67 eV out of a total 2.04 eV when considering all VNM (see Table S1), while the *combined* mode contributes to the remaining 0.37 eV.

Table S1. Grid parameters associated with the *main* and *combined* VNM. The total number of points computed for the *ab-initio* (ab) and ML grids results from the product of N_i^{ab} and N_i^{ML} (1323 and 26208, respectively).

Type	i	E_i^{vert}	Q_i^{MAX}	Q_i^{MIN}	N_i^{ab}	N_i^{ML}
main	1	0.24	1.05	−5.19	3	6
	2	0.22	5.03	−1.00	3	6
	8	1.09	16.01	−3.20	7	14
	24	0.12	0.51	−2.56	3	4
combined		0.37	-	-	7	13

At each point of the grid, we have evaluated the electronic enthalpy (H_{elec}^l) of the LS, IS and HS states using DFT (see Computational Details). The collection of LS, IS and HS energies provides a first estimation of the Potential Energy Surface of these states in the region contained between the minima. The resulting PES is, however, too sparse to be used in subsequent steps of the process (see discussion in Section S5). To increase the density of points, we generated a second grid that is evaluated using Machine Learning (ML) methods. The new grid is generated with the same procedure described above, but changing the parameter M (eq. S4) from 3.5 to 1.5, which results in $N_i = 6,6,14,4$ the four main modes (see Table S1). The *combined* mode is also evaluated in shorter intervals, with $N_C = 13$. The total number of points of this ML grid is 26208, which would represent a huge computational effort for *ab-initio* methods but is accessible to Machine Learning (ML) techniques. The size of the grid is maintained from section S1.1; the range of Q_i values is identical (Q_i^{MIN} and Q_i^{MAX}) as well as the *boundary* parameter (B in eq. S3a-b).

S1.2. Evaluation of the Free Energy at Grid Points

In section S1.1 we have described how we generated the grid in which the H_{elec}^l for the LS, IS and HS states has been computed. To incorporate the vibrational enthalpy and entropy contributions ($H_{vib,i}^l$ and $S_{vib,i}^l$), we have based our approach on the harmonic-oscillator expressions (eq. S6 and S7).

$$H_{vib,i}^l = \frac{1}{2}h\nu_i^l + \frac{h\nu_i^l}{e^{h\nu_i^l/k_BT} - 1} \tag{S6}$$

$$S_{vib,i}^l = \frac{h\nu_i^l}{T}\frac{1}{e^{h\nu_i^l/k_BT} - 1} - k_B ln\left(1 - e^{-h\nu_i^l/k_BT}\right) \tag{S7}$$

where l and i refer to the *state* and the ith vibrational normal mode, respectively (as in the main text). These expressions (or simpler ones) are routinely employed to incorporate vibrational contributions to the spin state energies of SCO transitions and,[1–3] in doing so, retrieve the total free energy G_{tot}^l as eq. S8.

$$G_{tot}^l = H_{elec}^l + \sum_i H_{vib,i}^l - T(\sum_i S_{vib,i}^l + S_{elec}^l) \tag{S8}$$

However, these expressions are meant to be applied at the minima (*i.e.* at $Q_{i,REF}^l$), using the corresponding set of VMN (ν_i^l) for each state. In this case, however, we aim at evaluating these contributions out of the minima, along the entire grid of points. To do so, the contributions of $H_{vib,i}^l$ and $S_{vib,i}^l$ have been modified as follows:

To start, it is indeed useful to discuss the application of the zero-point energy corrections (ZPE) under the same scenario. The ZPE corrections are the 0 K version of eq. S6 (see eq. S9), and its energy contribution at the minimum is the potential energy of the harmonic oscillator at its maximum extension ($Q_i^l = \pm1$, compare eq. S9 and eq. S10):

$$ZPE_i^l = \frac{1}{2}h\nu_i^l \tag{S9}$$

$$E_{Harm,i}^l = \frac{1}{2}h\nu_i^l Q_i^{l^2} \tag{S10}$$

The corrected (*i.e.* including ZPE) total energy of the harmonic oscillator within the $Q_i^l = \pm 1$ range is constant. For that to be true, the actual contribution of the ZPE correction to the total energy must decrease, when moving away from the minimum ($Q_i^l = 0$), following a parabola, as in eq. S11.

$$E_{ZPE,i}^l(Q) = E_{ZPE,i}^l(Q=0) - E_{Harm,i}^l = \frac{1}{2}h\nu_i^l - \frac{1}{2}h\nu_i^l Q_i^{l\,2} = \frac{1}{2}h\nu_i^l\left(1 - Q_i^{l\,2}\right) \tag{S11}$$

In our case, we assumed that the same parabolic decrease (or similar) can be applied to correct $H_{vib,i}^l$ out of the minima. To this purpose, we introduced a set of factors f_i^l, whose aim is to enforce this parabolic decrease. These factors are different for each state, for each point in the grid, and for each VNM, and were tentatively defined as in eq. S12.

$$
\begin{aligned}
\Delta Q_i^l = Q_i^l - Q_{i,REF}^l \\
\text{if } |\Delta Q_i^l| \le 1 \qquad\qquad f_i^l = 1 - \Delta Q_i^{l\,2} \\
\text{if } |\Delta Q_i^l| > 1 \qquad\qquad f_i^l = 0
\end{aligned}
\tag{S12}
$$

The factor effectively diminishes the $H_{vib,i}^l$ contribution of a given VNM as it moves away from the minimum, until it cancels its contribution if $|\Delta Q_i^l| > 1$. So, the contribution of a VNM to the vibrational enthalpy at any Q coordinate can be defined as:

$$H_{vib,i}^l(Q) = \frac{1}{2}h\nu_i^l\left(1 - \Delta Q_i^{l\,2}\right) = H_{vib,i}^l(Q=0)\cdot f_i^l \tag{S13}$$

This definition of f_i^l is valid as long as the total energy H_{elec}^l of a grid point (*i.e.* the computed one) corresponds to the energy of the minimum ($H_{elec,0}^l$), plus VNM contributions following the expression of the harmonic oscillator with ν_i^l ($E_{Harm,i}^l$) (eq. S14). That is, a perfectly harmonic case. As expected, this is not what happens in real molecules, and H_{elec}^l must be computed with ab initio or machine learning techniques, and not estimated from simple harmonic oscillator expressions.

$$H_{elec}^l = H_{elec,0}^l + \sum_i E_{Harm,i}^l \tag{S14}$$

Besides the impact of anharmonicity in H_{elec}^l, which is properly addressed by our computation of H_{elec}^l, we noticed two other effects that induce a deviation from a harmonic behaviour. The first one is second-order effects, or couplings between VNM. These occur when the frequency of a given VNM (ν_i^l) changes as the molecule moves in the direction of a second VNM (ν_j^l). The second effect only applies to the IS and HS states, and stems from our need to employ ω_i^l values (instead of ν_i^l) to describe them. That is, for the LS state we can use the eigenvalues of its diagonal hessian (ν_i^{LS}), but for the IS and HS states we need to rotate their hessian to match the basis of LS VNM, yielding a non-diagonal matrix. Non-zero non-diagonal values appear (ω_{ij}^l), and the diagonal values ($\omega_{ii}^l = \omega_i^l$) are generally larger than (ν_i^l). As a result of both effects, the energy at a given point of the grid deviates from the harmonic contributions evaluated with ν_i^l, and the expression of the factors has to be slightly adapted.

To retain the harmonic oscillator view as much as possible, while incorporating the aforementioned deviations, effective oscillator frequencies were defined ($\nu_{eff,i}^l$). These are small modifications to ν_i^l (or ω_i^l), and are calculated with the constrain that, when the harmonic oscillator expressions are applied, one recovers the computed energy at the grid point $H_{elec}^l(Q)$:

$$H_{elec}^l(Q) = H_{elec,0}^l + \sum_i E_{Anharm,i}^l(Q) = H_{elec,0}^l + \sum_i \frac{1}{2}\nu_{eff,i}^l \Delta Q_i^{l\,2} \tag{S15}$$

In practice, the difference between $\nu_{eff,i}^l$ and ν_i^l is very small (*ca.* 1%), except in soft-modes and those associated with large $|\Delta Q_i^l|$ values. With this approach, one also obtains the contribution of each VNM to the total energy, which we label as $E_{Anharm,i}^l$. Now, the definition of f_i^l can be updated to the final:

$$\text{if numerator} > 0 \qquad f_i^l = \left[H_{vib,i}^l(Q=0) - E_{Anharm,i}^l(Q) \right] / H_{vib,i}^l(Q=0)$$

$$\text{else:} \qquad f_i^l = 0 \qquad\qquad \text{(S16)}$$

Finally, these $\nu_{eff,i}^l$ are used to compute $H_{vib,i}^l$ in eq. S6, in combination with the associated f_i^l (eq. S16). In turn, $S_{vib,i}^l$ is computed directly using equation S7. For the reference LS state, the original ν_i^{LS} frequencies are used to compute $S_{vib,i}^l$, while for the IS and HS states, a different set of $\nu_{eff,i}^l$ is used, which accounts for the impact of rotating their hessian to match the basis of LS VNM, as explained above. Having this in mind, the final expression for G_{tot}^l at a given grid point is:

$$G_{tot}^l = H_{elec}^l + \sum_i (H_{vib,i}^l \cdot f_i^l) - T(\sum_i S_{vib,i}^l + S_{elec}^l) \qquad \text{(S17)}$$

S1.3. Example

Consider a VNM with $\nu_i^l = 200$ cm⁻¹ and $\nu_{eff,i}^l = 240$ cm⁻¹. At Q=0, we set $H_{elec,0}^l$ as 0, and $H_{vib,i}^l(Q=0)$ is $4.56 \cdot 10^{-4}$ atomic units (as a result of applying eq. S6). In the range of Q between 0 and ±2, $H_{elec}^l(Q)$ evolves as defined in equation S14 and shown in Figure S1. On top of it, $H_{vib,i}^l(Q)$ contributions are added with eq. S13. Adopting the f_i^l resulting from the harmonic oscillator (eq. S12), leads to $H_{vib,i}^l(Q)$ being smaller than $H_{elec}^l(Q)$ above Q=1, which is incorrect (see blue points below black points in Figure S1). This is caused by $\nu_{eff,i}^l$ being larger than ν_i^l due to anharmonicity. When using f_i^l as defined in eq. S16, we recover the expected evolution of $H_{vib,i}^l(Q)$ along this VNM, with a flat region close to the minimum where $H_{vib,i}^l(Q) = H_{vib,i}^l(Q=0)$, and the harmonic increase resulting from $H_{elec}^l(Q)$ at larger displacements. Notice that this is just a representation of how the factors are computed, and the type of behaviour we wanted to achieve. In the grid, $H_{elec}^l(Q)$ is evaluated with *ab initio* or machine learning methods, and $\nu_{eff,i}^l$ changes when moving along the corresponding VNM (ν_i^l) instead of being constant
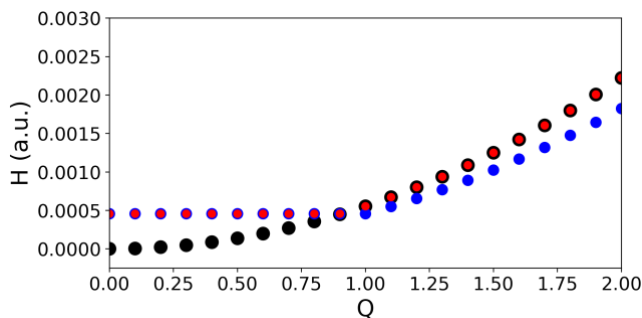
Figure S1. Example of the evolution of (**black**) $H_{elec}^l(Q)$ and of $H_{elec}^l(Q) + H_{vib,i}^l(Q) \cdot f_i^l$, with f_i^l defined as in equations (blue) S12 and (red) S16.

S2. Spin State Energetics of the SCO

Table S2. Comparison of thermodynamic values associated with the thermal SCO of **1** computed with different DFT methods. The experimentally-reported $T_{1/2}$ of crystals based on **1** range from 288 K in [Fe^{II}(1-bpp)$_2$][BF$_4$]$_2$·3H$_2$O to 171 K in [Fe^{II}(1-bpp)$_2$][PF$_6$]$_2$. For crystals of [Fe^{II}(1-bpp)$_2$][BF$_4$]$_2$, PBE+U computations have been performed under different approximations, and the impact of crystal packing effects were evaluated by comparing the HS-LS energy gap in gas phase (gp) and solid state (ss) conditions, using the optimized crystal geometries. Enthalpy values are given per molecule and in kJ·mol⁻¹ and entropy values in kJ·K⁻¹·mol⁻¹.

	Minimum (type)	ΔH_{elec}^{HS-LS}	$\Delta H_{vib}^{HS-LS}(T_{1/2})$	$\Delta S_{vib}^{HS-LS}(T_{1/2})$	$T_{1/2}$(K)	Ref.
1	B3LYP*	**24.0**	−3.0	60.8	283	this work
[Fe^{II}(1-bpp)$_2$][BF$_4$]$_2$	PBE+U+D2 (ss)	**19.1**	−1.9	52.8	259	1
[Fe^{II}(1-bpp)$_2$][BF$_4$]$_2$	PBE+U+D2 (gp)	**15.9**	-	-	-	1
[Fe^{II}(1-bpp)$_2$][BF$_4$]$_2$	PBE+U+D3BJ (ss)	**19.2**	−2.0	52.8	259	2
[Fe^{II}(1-bpp)$_2$][BF$_4$]$_2$	PBE+U+D3BJ (gp)	**20.6**	-	-	-	2
		ΔH_{tot}^{HS-LS}		$\Delta S_{vib}^{HS-LS}(T_{1/2})$	$T_{1/2}$(K)	Ref.
	Experiment	17.2		52.8	259	5

Compound **1** in the crystal [Fe^{II}(1-bpp)$_2$][BF$_4$]$_2$ has been studied with the PBE+U method in the solid state under different dispersion corrections.[1,2] The goal of these works was to benchmark the U parameter that had to be used to reproduce the energy

5

contributions reported experimentally. For this reason, ΔS_{vib}^{HS-LS} and $T_{1/2}$ match the experimental values. The PBE+U computations were performed at both the solid state (*ss* in Table S2), and gas phase (*gp*) levels on the same structure, the solid state minima, to evaluate the impact of intermolecular interactions on its energetics. These do not alter ΔH_{elec}^{HS-LS} significantly. Their contribution amounts 3.2 kJ/mol with PBE+U+D2 (19.1–15.9, see Table S2) and −1.4 kJ/mol with PBE+U+D3BJ (19.2–20.6, see Table S2).

S3. Structure of the MECP

Table S3. Comparison of minima and MECP structures. Given that the MECP evolve with temperature, the values shown are the averages among the number of MECP found along the entire set of temperatures explored.

Structure	avg. d(Fe-N) / Å	max. d(Fe-N) / Å	min. d(Fe-N) / Å	Σ / °	CShM
HS-LS MECP	2.110	2.155	2.034	115.65	3.715
HS-IS MECP	2.109	2.176	2.009	107.78	3.260
IS-LS MECP	2.133	2.195	2.038	115.99	3.746
HS Minimum	2.196	2.213	2.172	151.60	5.962
IS Minimum	2.111	2.177	1.980	107.04	3.225
LS Minimum	1.985	2.010	1.936	86.50	2.053

$\Sigma = \sum_{i=1}^{12} |90 - \beta_i|$; where β_i are the 12 cis N-Fe-N angles about the iron atom

The three types of MECP (HS/LS, HS/IS and IS/LS) are associated with similar values for the d(Fe-N), Σ and Continuous Shape Measures (CShM) descriptors, which in turn are similar to those of the IS minimum. Despite this fact, the MECP involving the IS are well above in energy than the HS/LS MECP. This suggests that other types of molecular motions that are not captured by the three chosen descriptors might be energetically relevant. We have selected these descriptors because they are especially suitable to capture changes in the first coordination sphere in the form of an elongation of the Fe-N distances, or a Jahn-Teller distortion.
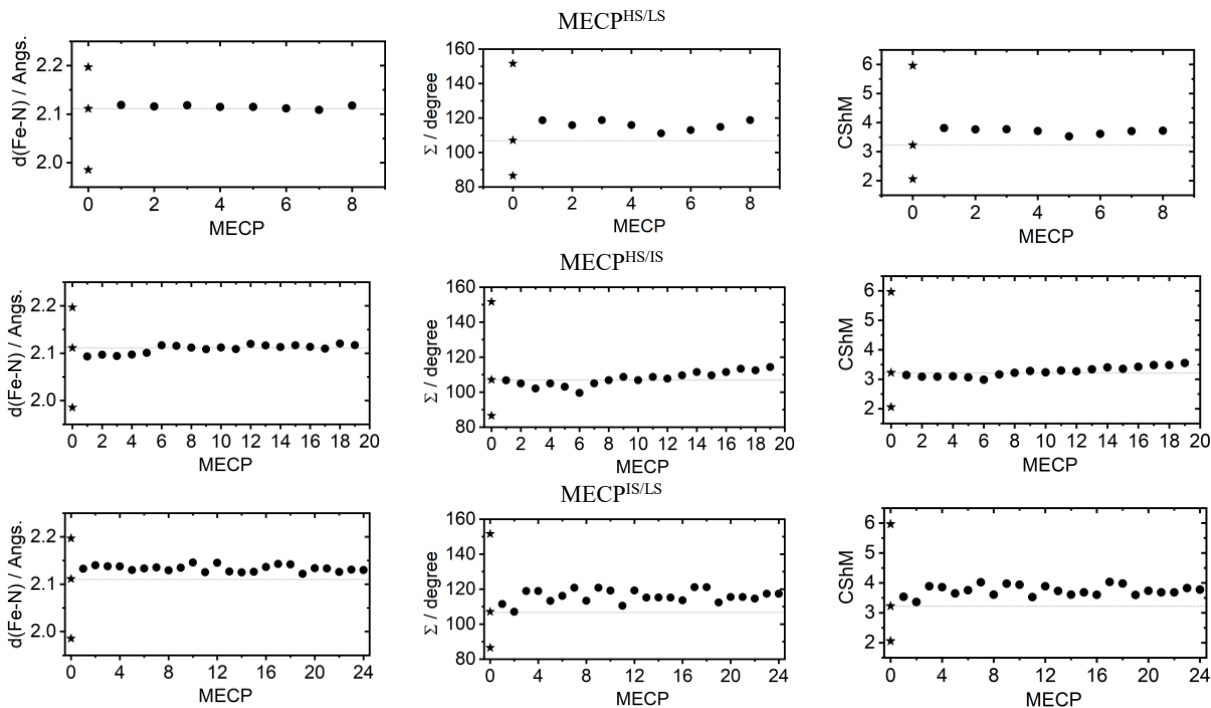
Figure S2. Evolution of the structural descriptors of the (top) HS-LS MECP, (middle) HS-IS MECP, and (bottom) IS-LS MECP along temperature. Values for the minima are indicated with stars (HS-above, IS-center, LS-below). The horizontal axis represents the different MECP connecting the HS and LS free-energy surfaces found along the range of temperatures explored (10-300K), ordered from low- to high-temperature.

S4. Temperature-Evolution of the Energy Barriers
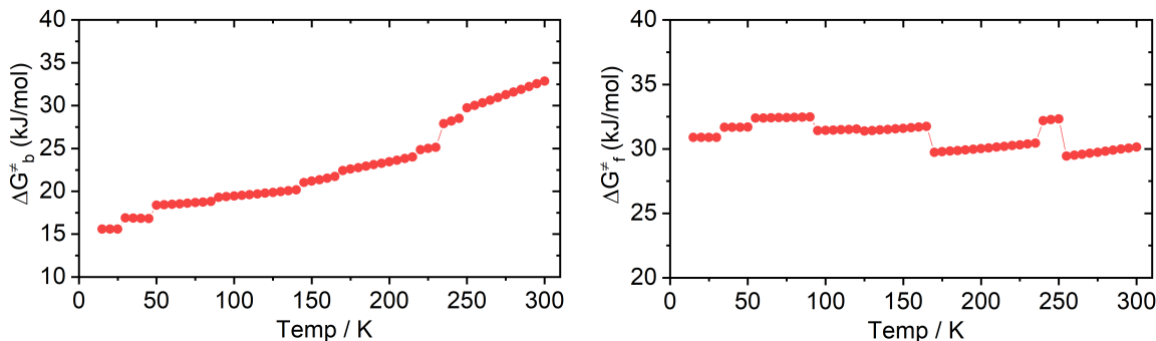
Figure S3. Activation energy for the (left) thermal LIESST relaxation process (*i.e.* $\Delta G_b^{\neq}$) and (right) the thermal SCO transition (*i.e.* $\Delta G_f^{\neq}$) in the *direct* pathways, obtained using the ML grid. Results on the "*ab initio*" grid are shown in Figure S6.

S5. Results using the *ab-initio* Grid

In section S1.1 we describe the initial "*ab-initio* grid" that is used as a starting point to generate the denser grid, which is evaluated using Machine-Learning (ML) methods ("*ML grid*"). In the main text, we directly describe the results obtained on the extended grid, but it might be illustrative to compare the results we obtain with the *ab-initio vs. ML* grids. With the *ab-initio* grid, we obtain $T_{LIESST} \approx 90\ K$ (*vs.* 80 K) for the *direct* pathway, $T_{LIESST} \approx 200\ K$ (*vs.* 195 K) for the *indirect* pathway, and $T_{1/2} = 265\ K$. The slightly higher T_{LIESST} stem from the fact that a smaller number of ECP are identified (from 3 at 10 K to 30 at 300 K), which implies that the MECP are higher in energy, and hence the kinetics are slower (*i.e.* larger τ_D and τ_I), so the temperature required to reach the second timescale (our definition of T_{LIESST} and $T_{1/2}$) is higher. The smaller number of ECP is not only due to the smaller number of grid points, but is also related to the methods ability to identify ECP. The problem is related to the fact that we evaluate the FES at specific points, instead of continuously. To illustrate our point, in Figure S4 we show a scheme of the evolution of hypothetical HS and LS FES that cross at a given point, an ECP. The left plot illustrates the case of a sparse grid, in which the FES are evaluated (circles) at equidistant steps quite separate from each other. The energy criterion ($\Delta G < k_B T$) is evaluated between points at the same geometry (*i.e.* same position in the horizontal axis, dotted lines in S4). In sparse grid (left), this criterion might fail at detecting an ECP if the FES are too steep, since the evaluated points adjacent to the ECP might be already too far apart in energy. A denser grid (right) can properly identify the ECP and provide an accurate energy evaluation (Figure S4).
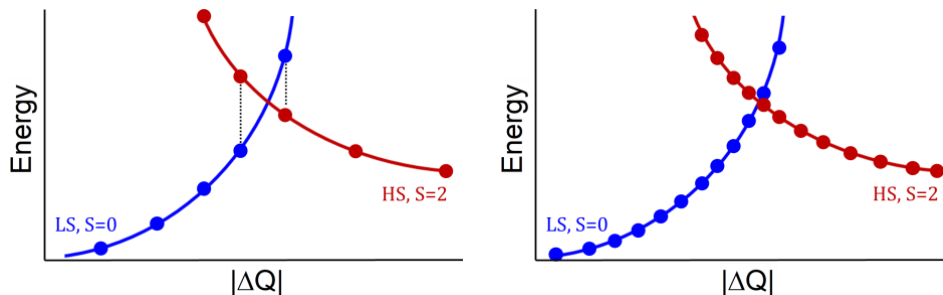
Figure S4. Representation of hypothetical HS and LS FES crossing at a point in space, an ECP. The circles represent grid points, characterized by ΔQ, at which the energy is evaluated. The dotted lines indicate that the energy criterion of $\Delta G < k_B T$ is evaluated between energies computed at the same point in ΔQ.

In practice, the difference in T_{LIESST} obtained with the *ab-initio vs*. ML grids is not very large (90 *vs.* 80 K, respectively). However, artefacts appear in the evaluation of the energy barriers ($\Delta G_b^{\neq}$, see Figure S5) and the half-life times (see Figure S6) with the sparser *ab-initio* grid, so the characterization of the MECP with the sparser *ab-initio* grid is far from optimal.
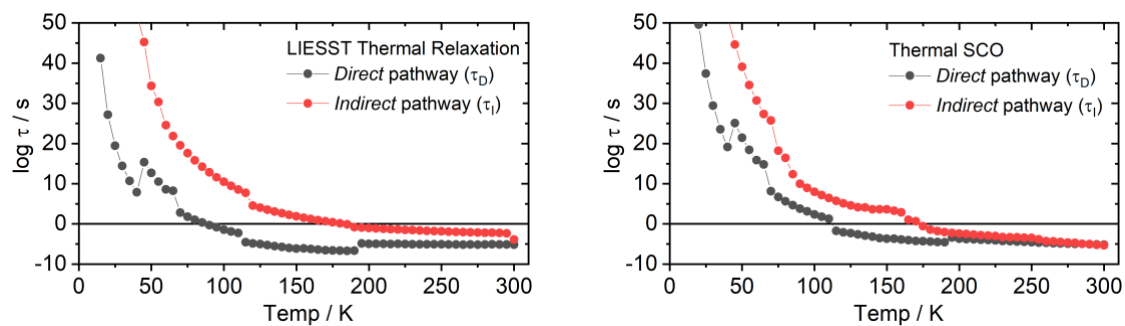
Figure S5. Temperature-evolution of the half-life times associated with the *direct* (τ_D) and *indirect* (τ_I) pathways for the (left) *forward* (LS-to-HS, *i.e.* thermal SCO) and (right) *backward* (HS-to-LS, *i.e.* LIESST) reactions, using the "*ab-initio*" grid. Results on the ML grid are shown in Figure 2 of main text.
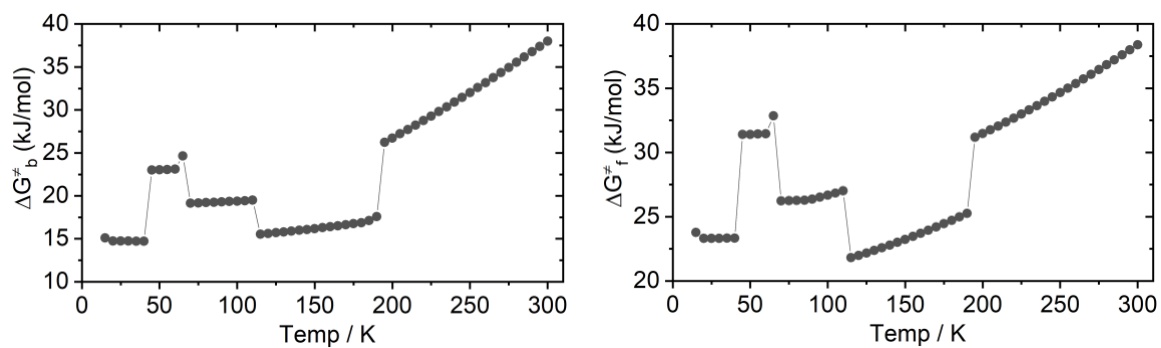
Figure S6. Activation energy for the (left) thermal LIESST relaxation process (*i.e.* $\Delta G_b^{\neq}$) and (right) the thermal SCO transition (*i.e.* $\Delta G_f^{\neq}$) obtained using the "*ab-initio*" grid. The results obtained with the ML grid are shown in Figure S3.

S6. Assessment on the Quality of the ML grid.

At this stage, it is worth mentioning few technical aspects related to the quality of the protocol presented in Section S1, and in particular to the quality of the grid. First, the MECP are always at the middle point of the space explored in any of the *main* and *combined* dimensions. Accordingly, in Figure 1 the MECP appear far from the extreme values of $|\Delta Q|$. This indicates that the grid is sufficiently large to find the relevant MECP. Second, the number of HS-LS ECP that are identified in the ML grid increases continuously from 25 at 10 K, to 150 at T_{LIESST}, and up to 500 at 300 K. Notice that grid points are classified as ECP if the energy difference lies below $k_B T$, which becomes a softer threshold at higher temperatures. Such high number of ECPs suggests that the grid is not only sufficiently large, but also sufficiently dense, to properly identify the MECP. Third, while the three types of MECP (HS/LS, HS/IS and IS/LS) are associated with similar values for the d(Fe-N), Σ and CShM descriptors, the IS is well above in energy than the HS/LS MECP. This suggests that other types of molecular motion that are not captured by d(Fe-N), Σ and CShM, might be energetically relevant, which reinforces our approach based on the exploration of the FES along the entire geometrical space instead of searching along predefined dimensions.
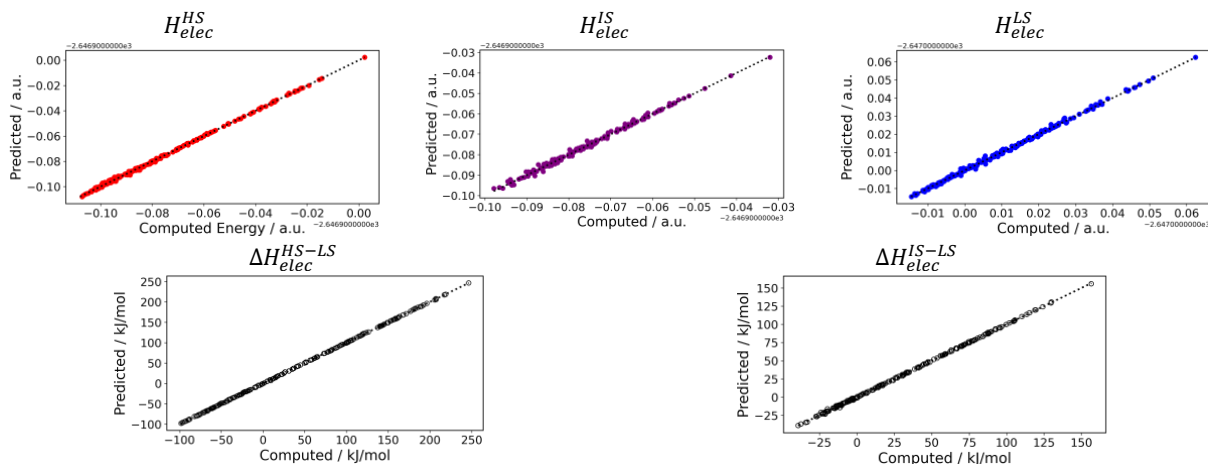
Figure S7. Comparison between computed and predicted H_{elec}^l values for 200 randomly selected geometries of the ML grid for the HS (red), IS (purple) and LS (blue) states. Also shown the relative energy differences between states. Diagonal black dashed lines indicate perfect correlation.

In Section S1.1, we describe the generation of the ML grid. The H_{elec}^l values for *l*=HS, IS, LS are evaluated with ML models. The MAE error associated with the ML prediction is evaluated on a test set of 200 randomly selected geometries by comparison with *ab-initio* results (at the B3LYP*-D3BJ/Def2-SVP level). The overall MAE is of around 1.3 kJ/mol, with little differences among spin states (1.3 kJ/mol for LS and HS, 1.4 kJ/mol for IS). These errors partially compensate when computing relative energy differences, so that ΔH_{elec}^{HS-LS} and ΔH_{elec}^{IS-LS} have MAE of 0.5 and 0.6 kJ/mol, respectively.

S7. Assessment on the TST parameters.

$$k = p_{sh} \cdot \frac{\kappa k_b T}{h} e^{-\frac{\Delta G^{\neq}}{RT}} \qquad\qquad (S18)$$

As discussed in the main text, the rate constants have been computed using the non-adiabatic version of TST proposed in ref. 6, and taking both the transmission coefficient (κ) and the hopping probability (p_{sh}) as 1. These parameters appear in the pre-factor of equation S18 and, as such, are less relevant than the energy barriers in the exponential part. Nevertheless, their value has an impact on the prediction of T_{LIESST} (less on $T_{1/2}$ as it is thermodynamically controlled). Changes in κ do shift the resulting T_{LIESST} by few K, but without relative changes between the different pathways. However, this is different for p_{sh}. Different hopping probabilities should ideally be used for the direct and indirect pathways, accounting for their different SOC. Approximate SOC values are 50 cm^{-1} for HS-IS and LS-IS crossings, and 1 cm^{-1} for HS-LS,[7] which would correspond to p_{sh}=0.0001 for the direct pathway and p_{sh}=0.01 for each of the two steps of the indirect pathway.[6] Using these values, we retrieve T_{LIESST}=134 K (*vs.* 80 K) for the direct pathway, and T_{LIESST}=286 K (*vs.* 195 K) for the indirect pathway. While the shift is significant in quantitative terms, it does not modify the conclusions we extract from the application of our protocol to compound **1**. Indeed, these shifts are largely compensated by choosing the minute or the hour timescale in the definition of T_{LIESST}, instead of the second timescale, which could compare even better with experimental timescales. Under the hour (minute) timescale, our T_{LIESST} predictions for the direct and indirect pathways with the modified p_{sh} are 85 K (104 K), and 200 K (241 K), very close to the values reported in the main text (80 K and 195 K) (see Table S4).

Table S4. Comparison of T_{LIESST} predictions of **1**, for the direct and indirect pathways under different combinations of the p_{sh} parameter within TST, and the timescale to assign T_{LIESST}. In bold, the combination discussed in the main text.

p_{sh}	timescale	T_{LIESST} direct pathway (K)	T_{LIESST} indirect pathway (K)
Standard (= 1.0)	**second**	**80**	**195**
Standard (= 1.0)	minute	66	142
Standard (= 1.0)	hour	57	132
Modified (= 0.01 and 0.0001)	second	134	286
Modified (= 0.01 and 0.0001)	minute	104	241
Modified (= 0.01 and 0.0001)	hour	85	200

ESI References

(1)   Vela, S.; Fumanal, M.; Ribas-Arino, J.; Robert, V. Towards an Accurate and Computationally-Efficient Modelling of Fe(II)-Based Spin Crossover Materials. *Phys. Chem. Chem. Phys.* **2015**, *17* (25). https://doi.org/10.1039/c5cp02502h.

(2)   Vela, S.; Fumanal, M.; Cirera, J.; Ribas-Arino, J. Thermal Spin Crossover in Fe(II) and Fe(III). Accurate Spin State Energetics at the Solid State. *Phys. Chem. Chem. Phys.* **2020**, *22* (9), 4938–4945. https://doi.org/10.1039/D0CP00162G.

(3)   Bucko, T.; Hafner, J.; Lebegue, S.; Angyan, J. G. Spin Crossover Transition of Fe(Phen)2(NCS)2: Periodic Dispersion-Corrected Density-Functional Study. *Phys. Chem. Chem. Phys.* **2012**, *14* (16), 5389–5396.

(4)   Bao, J. L.; Truhlar, D. G. Variational Transition State Theory: Theoretical Framework and Recent Developments. *Chem. Soc. Rev.* **2017**, 7548. https://doi.org/10.1039/c7cs00602k.

(5)   Holland, J. M.; McAllister, J. A.; Lu, Z.; Kilner, C. A.; Thornton-Pett, M.; Halcrow, M. A. An Unusual Abrupt Thermal Spin-State Transition in [FeL$_2$][BF$_4$]$_2$ [L = 2,6-di(pyrazol-1-yl)pyridine]. *Chem. Commun.* **2001**, No. 6, 577–578. https://doi.org/10.1039/b100995h.

(6)   Harvey, J. N. Understanding the Kinetics of Spin-Forbidden Chemical Reactions. *Phys. Chem. Chem. Phys.* **2007**, *9* (3), 331–343. https://doi.org/10.1039/B614390C.

(7)   Sousa, C.; Domingo, A.; de Graaf, C. Effect of Second-Order Spin–Orbit Coupling on the Interaction between Spin States in Spin-Crossover Systems. *Chem. Eur. J.* **2018**, *24* (20), 5146–5152. https://doi.org/10.1002/chem.201704854.